CHAPTER 13

Visualizing Chemical Reactions in Solution with Femtosecond X-ray Scattering

SHIN-ICHI ADACHI*[a,b] AND HYOTCHERL IHEE*[c,d]

[a]Institute of Materials Structure Science, High Energy Accelerator Research Organization (KEK), 1-1 Oho, Tsukuba, Ibaraki 305-0801, Japan; [b]Department of Materials Structure Science, School of High Energy Accelerator Science, The Graduate University for Advanced Studies, 1-1 Oho, Tsukuba, Ibaraki 305-0801, Japan; [c]Center for Nanomaterials and Chemical Reactions, Institute for Basic Science (IBS), Daejeon 305-701, Republic of Korea; [d]Department of Chemistry, KAIST, Daejeon 305-701, Republic of Korea
*E-mail: shinichi.adachi@kek.jp, hyotcherl.ihee@kaist.ac.kr

13.1 Introduction

Long-lived electronic excited states of photoactive molecules govern the functional efficiencies involved in their functional transitions. In fact, the fate of the excited molecules is often determined by the early stages of their photoinduced reactions, involving bond breaking and bond making, and therefore understanding the mechanism of the initial reaction steps leading to the functional transitions is of supreme importance. For several decades, ultrafast bond-breaking processes of various molecular systems have been studied intensively using a variety of time-resolved techniques.[1–5] Contrary to the case of the bond-breaking process, which is essentially a unimolecular

Energy and Environment Series No. 18
X-Ray Free Electron Lasers: Applications in Materials, Chemistry and Biology
Edited by Uwe Bergmann, Vittal Yachandra and Junko Yano

Published by the Royal Society of Chemistry, www.rsc.org

process and therefore can be initiated by laser photolysis in a synchronized manner, bond making is a bimolecular process that requires two reactant parties to meet each other in order to form a chemical bond. In such a case, its reaction rate is limited by slow diffusion of the reactants through the solvent, and thus the moment of the encounter of two parties cannot be synchronized with laser excitation. Therefore, it is difficult to initiate and follow the process with ultrafast time resolution.

In this respect, a gold oligomer complex, $[Au(CN)_2^-]_n$, can serve as a good model system.[6–11] Au(I) atoms in gold oligomer complexes have a closed-shell d^{10} electronic configuration with a low coordination number, thereby exhibiting a non-covalent interatomic interaction caused by the relativistic effect, which is termed aurophilicity.[9–11] Aurophilicity makes Au(I) atoms weakly bind to each other by van der Waals interactions, forming an aggregate complex, $[Au(CN)_2^-]_n$, without any covalent bond. In the viewpoint of the bimolecular reaction, the two reactant parties, *i.e.*, the $Au(CN)_2^-$ monomer, that are involved in the bimolecular reaction are already "prepared" in close proximity. Upon photoexcitation of the complex, an electron is excited from an antibonding $d_{z2}\sigma^*$ orbital to a bonding $p_z\sigma$ orbital, leading to the formation of covalent bonds among Au atoms.[7] Since Au atoms belong to the same solvent cage in the ground state of the $[Au(CN)_2^-]_n$ complex, the formation of Au–Au covalent bonds occurs without being limited by slow diffusion through the solvent. Therefore, the ultrafast time resolution can be achieved for probing this bond-making process as in typical unimolecular reactions synchronized with laser photolysis, but the ensuing reaction is a bimolecular reaction between $Au(CN)_2^-$ monomers.

Recently, ultrafast Au–Au bond formation in gold dimer and trimer complexes, $[Au(CN)_2^-]_2$ and $[Au(CN)_2^-]_3$, was investigated using transient absorption (TA) spectroscopy.[12,13] In the case of the gold trimer complex, the transient changes of absorption were observed with time constants of 500 fs, 2 ps and 2 ns. The first kinetic component (500 fs) was ascribed to the intersystem crossing to a triplet state, which is presumably preceded by rapid contraction of Au–Au bonds within 500 fs.[12] The second kinetic component (2 ps) was assigned to a conformational change from the bent to linear structure. It is worth noting that the second kinetic component (2 ps) is missing in the case of the dimer complex, suggesting that the 2 ps process is related to the intrinsic nature of the trimer complex.[13] Since the TA signal is not directly related to the molecular structure, those structural assignments were solely based on the theoretical electronic absorption spectra of model structures. Those structural assignments were disputed by a study using *ab initio* molecular dynamics simulation.[14] According to this study, the bent-to-linear transition occurs on a 500 fs time scale, although it was assigned to the 2 ps kinetic component in the TA study. Such a discrepancy between experiment and theory, mainly due to limited structural information obtained from experiments, is a rather common problem in chemistry in general. In order to resolve the discrepancy, we used time-resolved X-ray liquidography (TRXL), also known as time-resolved X-ray solution scattering (TRXSS), to elucidate

the ultrafast structural dynamics of Au–Au bond formation in $[Au(CN)_2^-]_3$ at the atomic level.[15,16]

TRXL, one of the time-resolved X-ray diffraction techniques,[17–49] is an effective method for probing photoinduced structural changes of molecules in solution and has been used for studying the dynamics and mechanisms of many molecular reaction systems, ranging from small molecules[25–39] to biological macromolecules.[40–49] Thus far, the temporal resolution of TRXL has been limited to only 100 ps, preventing the observation of ultrafast processes on the time scales of femtoseconds to picoseconds. This limit can be overcome with the recent development of X-ray free electron lasers (XFELs), which generate ultrashort (~100 fs long) X-ray pulses with ~10^{12} photons per pulse.[50–58] As a result, it has become possible to explore chemical processes occurring on the sub-picosecond time scale using TRXL. In this section, we describe the study of ultrafast structural dynamics of bond formation in $[Au(CN)_2^-]_3$ in solution with sub-picosecond time resolution and sub-angstrom spatial resolution by performing the TRXL experiment at both an XFEL facility and a synchrotron.

13.2 Experimental

The TRXL experiment is schematically shown in Figure 13.1. Scattering patterns, $S(q,t)$, from $[Au(CN)_2^-]_3$ solution were measured at various time delays up to 1 μs, including a reference time delay (−5 ps). By taking the difference between the scattering patterns measured at a positive time delay and the reference time delay, we obtained time-dependent difference scattering patterns, $\Delta S(q,t)$, which contain information on the structural change of reacting $[Au(CN)_2^-]_3$ molecules with all other contributions from non-reacting molecules removed. The contribution of solvent heating was determined by a separate experiment on a laser dye and subtracted from the experimental scattering curves with proper scaling.

13.2.1 Data Collection

TRXL data were collected at the BL3 beamline of SACLA and the NW14A beamline of KEK. X-Ray pulses with sub-100 fs duration generated from SACLA and 100 ps duration generated from KEK were used for measuring the data at early time delays (from −800 fs to 100 ps) and late time delays (from 100 ps to 1 μs), respectively. The reproducibility of the X-ray scattering signal at the two beamlines were checked by comparing time-resolved difference scattering curves, $q\Delta S(q,t)$, as shown in Figure 13.2.

The two difference scattering curves at a common time delay (100 ps) are identical to each other within the experimental error, indicating that our measurement is highly reproducible and independent of the facility. Difference scattering curves in the entire time range (from −800 fs to 1 μs) are shown in Figure 13.3.

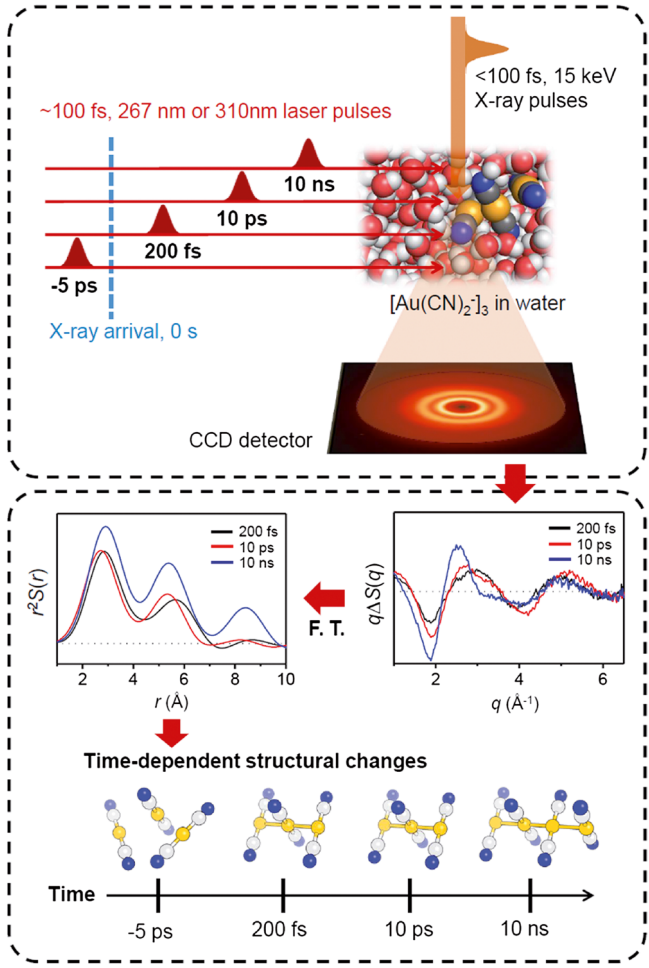

Figure 13.1 Schematic of femtosecond TRXL (top) and the data analysis (bottom). The photochemical reaction of solutes supplied by the liquid-flowing system is triggered by a femtosecond optical laser pulse. Subsequently, a time-delayed X-ray pulse synchronized with the laser pulse probes the structural dynamics of the reaction. The scattered signal is detected by a fast two-dimensional (2D) CCD detector. Solvent contributions were subtracted by taking the Fourier transform and compensating the depletion of the initial solute contribution due to the photochemical reaction. We obtained radial distribution functions (RDFs) in real space, which display the interatomic distances of transient species and products. As a result, the Au–Au bond lengths of the $[Au(CN)_2^-]_3$ complex were identified with sub-angstrom accuracy, providing the time-dependent structural changes of the metal complex in real time. Reprinted by permission from Macmillan Publishers Ltd: *Nature* (ref. 15), copyright (2015).

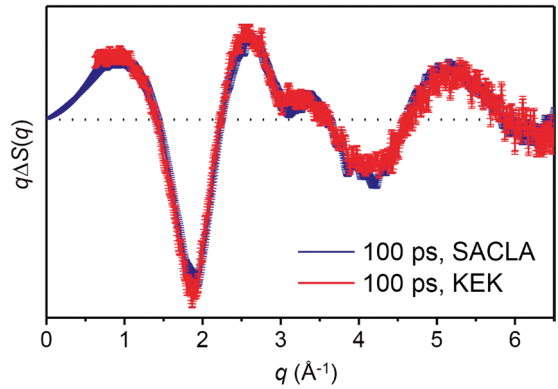

Figure 13.2 Comparison of the difference scattering curves at a common time delay, 100 ps, measured at SACLA (blue) and KEK (red). The two curves are nearly identical to each other within the experimental error, indicating that the difference scattering curves are highly reproducible and independent of the facility. Reprinted by permission from Macmillan Publishers Ltd: *Nature* (ref. 15), copyright (2015).

13.2.1.1 Data Collection at SACLA

TRXL measurement at early time delays (−800 fs–100 ps) was performed at the BL3 beamline of SACLA. Femtosecond laser pulses at 800 nm were generated from the Ti:sapphire regenerative amplifier and converted to the pulses at 267 nm or 310 nm wavelength. The laser beam was focused by a lens, where the laser beam was overlapped with the X-ray beam with the crossing angle of 10°. The 267 nm laser pulses were focused to a spot of 300 μm diameter, yielding a fluence of 2.1 mJ mm^{-2}, and the 310 nm laser pulses were focused onto a spot of 0.095 × 0.12 mm^2 size, giving the fluence of ~2 mJ mm^{-2}. The femtosecond X-ray pulses were generated from the XFEL at SACLA by self-amplified spontaneous emission (SASE). The X-ray pulses have narrow energy bandwidth ($\Delta E/E$ = 0.6%), a pulse duration of <100 fs, a center energy of 15 keV and a photon flux of ~10^{11} photons per pulse. We used an aqueous solution of the oligomer of the gold complex, $[Au(CN)_2^-]_n$. The aggregation number of the gold oligomer and the position of an absorption peak in the ultraviolet (UV) region change depending on the concentration of the sample solution. In this work, we focus on the trimer, $[Au(CN)_2^-]_3$, which is formed in a solution of 300 mM concentration and can be excited by the laser pulses of 267 nm or 310 nm. Upon photoexcitation, the trimer undergoes structural changes, including variation of its geometric structure and the formation of Au–Au covalent bonds. The solution sample was circulated through a sapphire nozzle with 100 μm-thick aperture to supply fresh sample for every laser shot. The structural change was monitored by the scattering pattern generated by X-ray pulses and measured with an area detector (Rayonix LX255-HS). The time resolution of the TRXL experiment was ~500 fs, which was limited by the timing jitter between the laser and X-ray pulses.

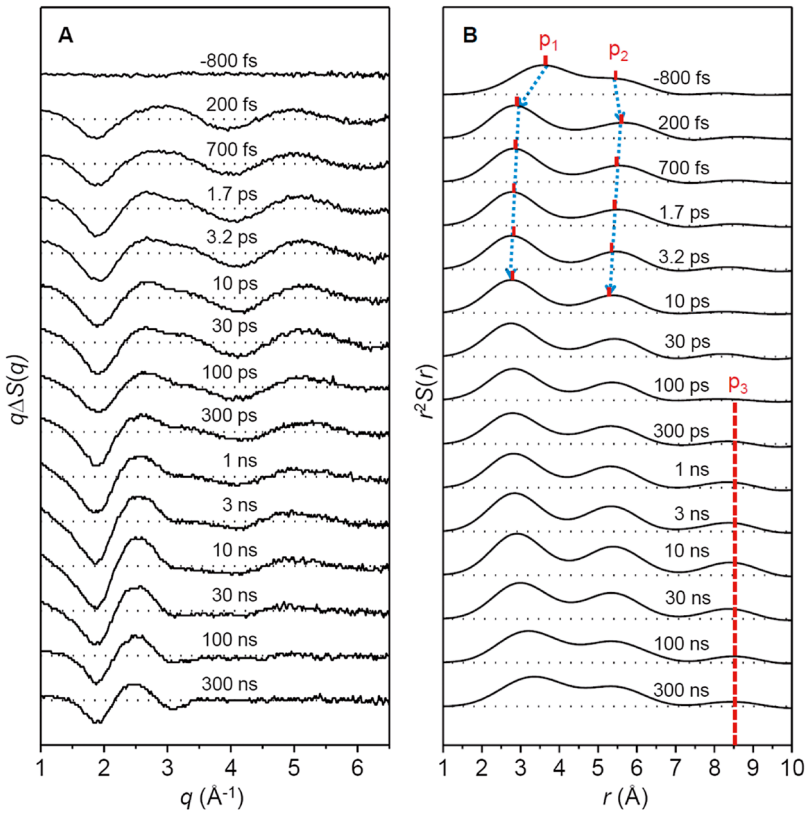

Figure 13.3 TRXL data of $[Au(CN)_2^-]_3$. (A) Experimental difference scattering curves, $q\Delta S(q)$, measured at various time delays from −800 fs to 300 ns. Data at only selected time delays are shown for clarity. (B) Radial distribution functions, $r^2S(r)$, obtained by sine-Fourier transformation of $q\Delta S(q)$ after subtracting solvent contributions. The RDF of the S_0 state was added to the RDFs at all time delays to emphasize only the contributions of the transient solute species associated with the bond formation. Reprinted by permission from Macmillan Publishers Ltd: *Nature* (ref. 15), copyright (2015).

The laser-off images were acquired with the laser pulse arriving 5 ps later than the X-ray pulse (that is, −5 ps time delay) in order to probe the (unexcited) molecules in the ground state while assuring the same average temperature of the sample solution. These laser-off images were used as a reference for calculating the time-resolved difference X-ray scattering patterns. To achieve a high enough signal-to-noise ratio for data analysis, about 50 images were acquired at each time delay. The scattering curves were measured at the following time delays: −5 ps, −800 fs, −300 fs, 200 fs, 700 fs, 1.2 ps, 1.7 ps, 3.2 ps, 5.2 ps, 10 ps, 20 ps, 30 ps, 50 ps and 100 ps. Time zero was determined by fitting the time trace of the difference scattering data for the sample solution with a convolution of a Gaussian function representing an instrument

response function (IRF) and the sum of exponential functions representing the transition dynamics among intermediate states. The scattering signals arising from solvent (water) heating were also measured using a 40 mM $FeCl_3$ solution with the same experimental conditions.

13.2.1.2 Data Collection at KEK

The TRXL measurement at late time delays (100 ps–1 μs) was performed at the NW14A beamline of KEK. The laser pulses with a center wavelength of 267 nm or 310 nm were focused onto a spot, where the laser beam overlapped with the X-ray beam with a crossing angle of 10°. The 267 nm laser pulses were focused to a spot of 300 μm diameter, yielding a fluence of 3.67 mJ mm^{-2}, and the 310 nm laser pulses were focused onto a spot of 0.343 × 0.492 mm^2 size, giving the fluence of ~0.2 mJ mm^{-2}. The laser pulses were synchronized with X-ray pulses from the synchrotron by an active feedback control loop that adjusts the laser oscillator cavity length, and the relative time delay between the laser and X-ray pulses was controlled electronically. The time-delayed X-ray pulses were selected by using a synchronized mechanical chopper. A multilayer optic coated with depth-graded Ru/C layers (d = 40 Å; NTT Advanced Technology, Japan) produced a Gaussian-type X-ray spectrum with a center wavelength of 0.83 Å and ~5% energy bandwidth. The scattering patterns generated by X-ray pulses of 100 ps (full width at half maximum, FWHM) duration were measured with an area detector (MarCCD165, Mar USA) with a sample-to-detector distance of 40 mm. The sample solution with the same concentration as used at SACLA was circulated through the sapphire nozzle with a 300 μm-thick aperture. The laser-off images were acquired with the X-ray pulse arriving 3 ns earlier than the laser pulse (that is, −3 ns time delay) in order to eliminate the contribution of the (unexcited) ground-state reactants. These laser-off images were used as a reference for calculating the time-resolved difference X-ray scattering patterns. To achieve a high enough signal-to-noise ratio for data analysis, more than 50 images were acquired and averaged at each time delay. The scattering curves were measured at the following time delays: −3 ns, −150 ps, 100 ps, 150 ps, 300 ps, 1 ns, 3 ns, 10 ns, 30 ns, 100 ns, 300 ns and 1 μs. The scattering signals arising from solvent (water) heating were also measured using a 40 mM $FeCl_3$ solution with the same experimental conditions.

13.2.2 Data Processing

13.2.2.1 Removal of the Solvent Contribution

In order to study only the dynamics of the Au–Au bond formation, the scattering arising from heating of pure solvent induced by laser excitation was subtracted from the experimental scattering data. The water heating signal was obtained by a separate solvent heating experiment on an $FeCl_3$ solution

at the same time delays used for the $[Au(CN)_2^-]_3$ solution. Singular value decomposition (SVD) of the data identified only one component, implying that only a single difference scattering curve accounts for the contribution of solvent heating in the time range up to 100 ps. In addition, the difference scattering curve of the $[Au(CN)_2^-]_3$ solution at 1 μs time delay is identical to the one for solvent heating, confirming that the difference scattering curves of $[Au(CN)_2^-]_3$ at late time delays are dominated by the solvent heating contribution due to reversibility of the reaction. The amount of heat dissipated in the sample solution can be determined from the scaling between these two curves. The obtained solvent heating contribution was subtracted from the experimental difference scattering curves at all time delays. The resultant difference scattering curve obtained by subtracting the solvent heating contribution can be regarded as the solute-only term because the contribution of the cage term (= solute–solvent cross term) is negligibly small.

13.2.2.2 Sine-fourier Transformation of qΔS(q)

The difference radial distribution function, $r^2\Delta S(r,t)$, is a measure of the radial electron density change as a function of interatomic distance r in real space and was obtained by sine-Fourier transformation of the $q\Delta S(q,t)$ curves:

$$r^2\Delta S(r,t) = \frac{r}{2\pi^2}\int_0^\infty q\Delta S(q,t)\sin(qr)e^{-q^2\alpha}dq, \qquad (13.1)$$

where the constant α (α = 0.03 Å^2) is a damping term that accounts for the finite q range in the experiment. Difference RDFs represent the change of Au–Au interatomic distance in the molecules participating in the reaction, and thus provide an intuitive picture of change in the molecular structure.

13.2.3 Data Analysis

13.2.3.1 SVD

As the step for determining the kinetic model of the photoinduced reaction of $[Au(CN)_2^-]_3$ and obtaining the species-associated RDFs for each transient state, we applied the SVD analysis to our experimental RDFs. From the TRXL data, we can build an $n_r \times n_t$ data matrix, **A**, where n_r and n_t are the number of r points in the RDFs and the number of time-delay points, respectively. Matrix **A** is decomposed into three matrices satisfying the relationship of $\mathbf{A} = \mathbf{USV}^T$, where **U** is an $n_r \times n_t$ matrix whose columns are time-independent r-spectra, also called left singular vectors (lSVs), **V** is an $n_t \times n_t$ matrix whose columns are amplitude changes of **U** as time evolves, also called right singular vectors (rSVs), and **S** is a diagonal $n_t \times n_t$ matrix whose diagonal elements are called singular values and can possess only non-negative values. The matrices **U** and **V** follow the relationships of $\mathbf{U}^T\mathbf{U} = \mathbf{I}_{n_t}$ and $\mathbf{V}^T\mathbf{V} = \mathbf{I}_{n_t}$, respectively, where $\mathbf{I}_{n_t}$ is the identity matrix. The diagonal elements of **S** (*i.e.*, singular values)

represent the weight of lSVs in **U**. Since the singular values are ordered so that $s_1 \geq s_2 \geq \ldots \geq s_n \geq 0$, both lSVs and rSVs on the more left or right are supposed to have larger contributions to **A**. The lSVs, when linearly combined together, give information on the RDFs associated with distinct transient species, while the rSVs contain information on the population dynamics of the transient species. Thus, the SVD analysis provides a model-independent estimation of the number of structurally distinguishable transient species and the dynamics of each species.

By performing the SVD analysis on our experimental difference RDFs, $r^2S(r,t)$, we identified four singular components with significant singular values, indicating the existence of four structurally distinguishable transient states. The rSVs of these four significant singular components were fitted by a convolution of a Gaussian function representing IRF and a sum of three exponential functions representing transitions among the transient intermediate states. As a result, we obtained the exponentials with the time constants of 1.6 (±0.1) ps, 3 (±0.5) ns and 100 (±20) ns, and an IRF with 480 fs (±10) fs width (FWHM). Thus, we identified four transient states and three kinetic components connecting the four species.

13.2.3.2 Kinetic Analysis

In order to obtain the species-associated RDFs of the four transient states identified in the SVD analysis, we performed kinetic analysis on the **U** and **V** matrices using an appropriate kinetic model. First, following the result of the SVD analysis, we defined new matrices, **U′**, **V′** and **S′**, that contain only the first four elements of **U**, **V** and **S**. In other words, **U′** is an $n_r \times 4$ matrix containing only the first four left singular vectors of **U**; **S′** is a 4×4 diagonal matrix containing only the first four singular values of **S**; and **V′** is an $n_t \times 4$ matrix containing the first four right singular vectors of **V**. Among various kinetic models, the only kinetic model that can account for the four transient states and the three kinetic components is the sequential model. Therefore, by solving rate equations based on the sequential model, the concentrations of the four transient states can be calculated using the three kinetic components determined from the SVD analysis. We defined a matrix **C** that represents the time-dependent concentrations of the four transient states and related it to **V′** using a parameter matrix **P** that satisfies the relationship of **V′ = CP**. In other words, the linear combination (by **P**) of the concentrations of the four transient states (**C**) gives the four rSVs constituting **V′**. In our analysis, **C** is an $n_t \times 4$ matrix containing the time-dependent concentrations of the four transient states denoted as S_0, S_1, T_1 and tetramer states, and **P** is a 4×4 matrix containing coefficients for the time-dependent concentrations of the transient states. Once we determine **C** by solving the rate equations and convoluting with the IRF, the theoretical RDFs at various time delays, **A′**, can be generated as follows.

$$\mathbf{A'} = \mathbf{U'S'V'}^{\mathrm{T}} = \mathbf{U'S'(CP)}^{\mathrm{T}} = \mathbf{U'S'(P}^{\mathrm{T}}\mathbf{C}^{\mathrm{T}}) = (\mathbf{U'S'P}^{\mathrm{T}})\mathbf{C}^{\mathrm{T}} \qquad (13.2)$$

The matrix **P** can be optimized by minimizing the discrepancy χ^2 between the theoretical and experimental difference scattering curves using the Minuit library:

$$\chi^2 = \sum_{i=1}^{n_r}\sum_{j=1}^{n_t}\left(\frac{r^2\Delta S_{\text{exp}}(r_i,t_j) - r^2\Delta S_{\text{theory}}(r_i,t_j)}{\sigma_{ij}}\right)^2, \tag{13.3}$$

where $r^2\Delta S_{\text{exp}}(r_i,t_j)$ and $r^2\Delta S_{\text{theory}}(r_i,t_j)$ are the experimental and theoretical RDFs at given r and t values, respectively, and σ_{ij} is the experimental standard deviation at given r and t values. From eqn (13.2), we can define a matrix **B** as $\mathbf{B} = \mathbf{U'S'P}^{\text{T}}$, that is, a linear combination (by **P**) of the four lSVs constituting **U′** that are weighted by their singular values in **S′**. As a result, matrix **B**, an $n_r \times 4$ matrix, contains the RDFs directly associated with the transient states. Thus, by optimizing matrix **P**, we obtain the time-independent, species-associated RDFs of the intermediate species (optimized **B**).

13.2.3.3 Calculation of Theoretical Radial Distribution Functions

For individual transient states, theoretical RDFs were expressed as a sum of multiple RDFs, S_{R_i}, each of which corresponds to an Au–Au pair,

$$r^2S_{\text{theory}}(r) = r^2\sum_{i=1}^{n} S_{R_i}(r), \tag{13.4}$$

where R_i is the Au–Au distance for an ith pair of Au atoms. For the trimer states (S_0, S_1 and T_1) and the tetramer, n was set to be three and six, respectively. Each $S_{R_i}(r)$ curve was calculated by sine-Fourier transformation of the theoretical scattering curve, $S_{R_i}(q)$, as follows:

$$r^2S_{R_i}(r) = \frac{r}{2\pi^2}\int_0^\infty qS_{R_i}(q)\sin(qr)\text{e}^{-q^2\alpha}\text{d}q. \tag{13.5}$$

The damping constant (α) used for obtaining the experimental RDFs was also used to obtain the theoretical RDFs. The theoretical scattering curves $S_{R_i}(q)$ from Au–Au pairs were obtained by the simple Debye formula,

$$S_{R_i}(q) = F_{\text{Au}}^2(q)\frac{\sin qR_i}{qR_i}, \tag{13.6}$$

where F_{Au} is the atomic form factor of the gold atom. By substituting eqn (13.5) and (13.6) into eqn (13.4), we obtained:

$$r^2S_{\text{theory}}(r) = \sum_{i=1}^{n}\frac{r}{2\pi^2}\int_0^\infty qF_{\text{Au}}^2(q)\frac{\sin qR_i}{qR_i}\sin(qr)\text{e}^{-q^2\alpha}\text{d}q. \tag{13.7}$$

The theoretical RDFs for the transient states were calculated by eqn (13.7). We note that the only variables in eqn (13.7) are the Au–Au distances.

13.2.3.4 Structural Fitting Analysis

To reconstruct the structures of the four states (S_0, S_1, T_1 and the tetramer) and extract the Au–Au distances for each state, we performed structural fitting analysis of the species-associated RDFs of the four states. As fitting parameters of the analysis, we considered three Au–Au distances for the S_0, S_1 and T_1 states, six Au–Au distances for the tetramer, and a scaling factor between the number of excited molecules and the signal intensity. It should be noted that we did not use any structural constraint that might impose a certain structure or symmetry. The maximum likelihood estimation (MLE) with the χ^2 estimator was employed with four (for S_0, S_1 and T_1 states) or seven (for tetramer) variable parameters. The chi-square (χ^2) is given by eqn (13.8):

$$\chi^2\left(R_1, R_2, R_3, A\right) = \frac{1}{N-p-1}\sum_i \frac{\left(S_{\text{theory}}\left(r_i\right) - S_{\text{exp}}\left(r_i\right)\right)^2}{\sigma_i^2}, \qquad (13.8)$$

where N is the total number of r points (= 500), p is the number of fitting parameters (= 4 or 7) and σ_i is the standard deviation. The likelihood (L) is related to χ^2 by eqn (13.9):

$$L(R_1, R_2, R_3, A) \propto \exp(-\chi^2/2). \qquad (13.9)$$

The errors of the multiple fitting parameters can be determined from this relationship by calculating the boundary values at 68.3% of the likelihood distribution. The calculation was performed by using the MINUIT software library and the error values were provided by the MINOS algorithm in MINUIT. Since we used the standard deviation of the measurement when calculating χ^2, the quality of the fit becomes better as the χ^2 approaches one.

13.2.3.5 Determination of RDF of the S_0 State

Time-independent species-associated difference RDFs of the transient states were obtained by the SVD and kinetic analyses of the experimental (time-dependent) difference RDFs. These difference RDFs correspond to $r^2(S_{S_0}(r) - S_{S_0}(r))$, $r^2(S_{S_1}(r) - S_{S_0}(r))$, $r^2(S_{T_1}(r) - S_{S_0}(r))$ and $r^2(S_{\text{tetramer}}(r) - S_{S_0}(r))$. From the structural fitting analysis described in Section 13.2.3.4, we were able to determine not only the RDFs of the transient states (S_1, T_1 and the tetramer) but also the RDF of the S_0 state. We used a common S_0 structure when fitting the four species-associated difference RDFs. By optimizing the fit between the experimental and the theoretical difference RDFs for each transient species, we were able to obtain the theoretical RDF of the S_0 state in addition to the RDFs of the other states. In order to emphasize only the contributions of transient solute species associated with the bond formation, we added the RDF of the S_0 state to the experimental difference RDFs at all time delays and obtained RDFs, $r^2S(r,t)$.

13.3 Results and Discussion

A comparison of the data obtained with excitation at two different wavelengths (267 and 310 nm) shows that the results are independent of excitation wavelength. Thus, hereafter we show the TRXL data at 267 nm excitation, which has better data statistics.[15,16] Experimental difference scattering curves, $q\Delta S(q,t)$, measured at various time delays from −800 fs to 300 ns are shown in Figure 13.3A. The difference scattering curves show distinct oscillatory features along the q axis, indicative of a large structural change of $[Au(CN)_2^-]_3$ during the formation of Au–Au covalent bonds. Considering that the oscillatory features appear distinct even at the earliest time delay (200 fs) of our measurement, the first step of the bond formation in $[Au(CN)_2^-]_3$ must occur impulsively within the time resolution of our experiment (~500 fs). The oscillatory features change further over time and almost disappear after 300 ns with only the contribution from solvent heating remaining thereafter.

A more intuitive picture of the structural change of $[Au(CN)_2^-]_3$ can be obtained by converting $q\Delta S(q,t)$ into difference RDFs, $r^2\Delta S(r,t)$, in r-space by sine-Fourier transformation. In order to emphasize the contributions of transient solute species associated with the bond formation alone, the RDF of the ground (S_0) state was added to the difference RDFs at all time delays, yielding $r^2S(r,t)$, as shown in Figure 13.3B. Since the solvent contributions were eliminated and the contributions from carbon and nitrogen atoms in $[Au(CN)_2^-]_3$ are almost negligible compared with the strong scattering from Au atoms, RDFs shown in Figure 13.3B actually represent the interatomic distances among the gold atoms of $[Au(CN)_2^-]_3$ in real space.

Two peaks denoted as p_1 and p_2 are distinct in the RDFs in Figure 13.3B. Considering that $[Au(CN)_2^-]_3$ is a trimer and the intensity of p_1 is about twice as large as p_2, we can assign p_1 to the Au_1–Au_2 (R_{12}) and Au_2–Au_3 (R_{23}) pairs, and p_2 to the Au_1–Au_3 pair (R_{13}). In the S_0 state (*i.e.*, RDF at −800 fs time delay), R_{12} and R_{23} (~3.6 Å as indicated by the position of p_1) are relatively large compared with the typical length of an Au–Au covalent bond (~2.7 Å), and R_{13} (~5.6 Å as indicated by the position of p_2) is smaller than the sum of R_{12} and R_{23}, indicating weakly bound Au atoms and a bent structure, respectively. As expected in the q-space data, the RDF at 200 fs time delay is significantly different from the one at −800 fs, suggesting that the first step of the bond formation in $[Au(CN)_2^-]_3$ occurs within the time resolution of our experiment. Compared to the S_0 state, R_{12} and R_{23} decrease significantly, indicating the formation of Au–Au covalent bonds at this step. Simultaneously, R_{13} (~5.6 Å) becomes similar to the sum of R_{12} and R_{23} (~2.8 Å each), which is evidence of a conformational transition from bent to linear geometry. We note that the time scale of the bent-to-linear transition determined from our TRXL experiment is in good agreement with the time scale predicted from the previous theoretical study.[14] From 200 fs to 10 ps, p_1 and p_2 shift to smaller distances, indicating further decrease of Au–Au distances due to the formation of stronger Au–Au covalent bonds. In this time range, the ratio between (R_{12} + R_{23}) and R_{13} remains at 1 : 1, indicating that the linear structure is preserved.

After 100 ps, p_3 appears at ~8.5 Å and grows up until 10 ns. Since the position of p_3 is too large for the Au–Au distance in the trimer complex, p_3 must be a signature of the formation of a tetramer complex. Also, increased intensities of p_1 and p_2 account for a larger number of Au–Au pairs present in the tetramer. After 10 ns, the RDF returns gradually back to the RDF of the S_0 state.

By SVD and principal component analysis (PCA), we obtained species-associated RDFs for four states assigned as S_0, S_1, a triplet (T_1) and tetramer, and their kinetics. We fitted the experimental RDFs at various time delays by linear combinations of the species-associated RDFs, and determined the time-dependent concentration of each state (Figure 13.4A). As a result, we obtained three kinetic components with time constants of 1.6 (±0.1) ps, 3 (±0.5) ns and 100 (±20) ns, which correspond to the transition from S_1 to T_1, the transition from T_1 to the tetramer, and the transition from the tetramer to S_0, respectively. The obtained values are summarized in Table 13.1.

The time scales of the three kinetic components match well with the ones identified in the previous TA study,[12] except that our TRXL data lack the ~500 fs component, which was assigned to intersystem crossing to a triplet state in the TA study. Here, we note that the 500 fs component was assigned to the S_1-to-T_1 intersystem crossing in the TA study but was not observed by TRXL. This discrepancy suggests that the intersystem crossing, if the assignment in the TA study is correct, does not involve any significant structural change detectable by TRXL, and thus we termed the initially formed T_1 state as T_1', which is structurally indistinguishable from S_1.

The reconstructed structures of the four states from structural fit analysis presented in Figure 13.4B and Table 13.2 are in good agreement with the structural changes inferred from Figure 13.3B. In the S_0 state, R_{12} and R_{23} are relatively large and R_{13} is smaller than the sum of R_{12} and R_{23}, indicating weakly bound Au atoms and the bent structure of the S_0 state. R_{12} and R_{23} are different from each other, which can be attributed to the asymmetric structure of the S_0 state or broadening of the RDF induced by the relatively free movements of weakly bound Au atoms if the S_0 state were symmetric. In the S_1 state, the Au–Au distances become considerably shorter, indicating that Au–Au bonds become stronger with covalent character. R_{13} in the S_1 state becomes longer than the one in the S_0 state and is identical to the sum of R_{12} and R_{23}, revealing that the conformational transition from bent to linear structure occurs in the S_1 state. In addition, R_{12} and R_{23} are identical to each other within experimental error despite the lack of any constraint on the two variables, indicating that the structure of the S_1 state is symmetric. As the S_1 state transforms to the T_1 state, the Au–Au distance further decreases with the linear and symmetric structure maintained, implying the formation of strong Au–Au covalent bonds. Since this process (further contraction of Au–Au bond in 2 ps) is missing in the case of the dimer complex,[13] the structural change is originated from the intrinsic nature of the trimer complex, which will be the subject of future study. Later, the trimer reacts with a free $Au(CN)_2^-$ monomer to form a tetramer, $[Au(CN)_2^-]_4$, before ultimately returning to the S_0 state. The changes in the Au–Au distances and the conformations of the

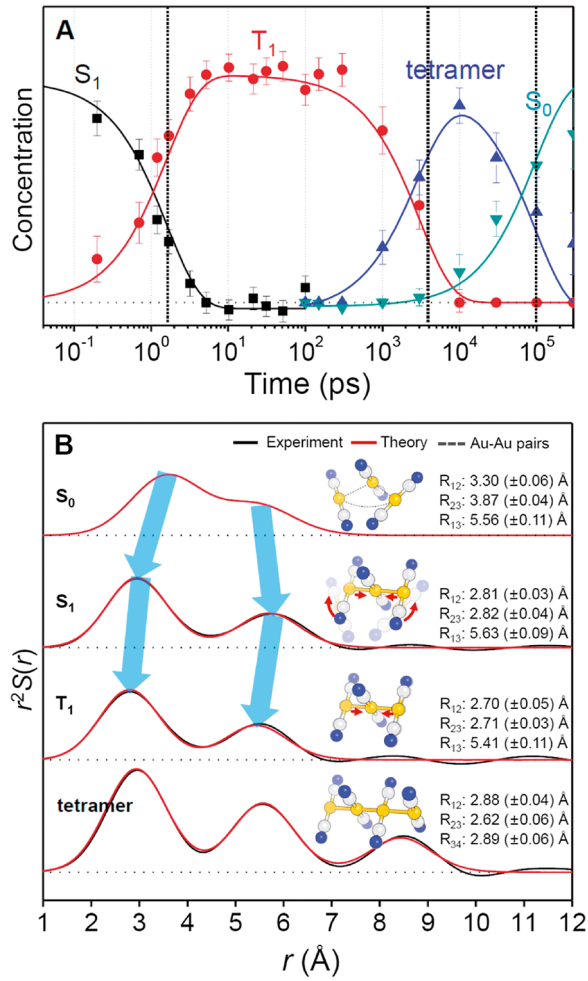

Figure 13.4 Time-dependent structural changes of $[Au(CN)_2^-]_3$. (A) Time-dependent concentrations of the four states and their transition kinetics. The name of each species is indicated above each trace. (B) Species-associated RDFs of the four structures obtained from the SVD and PCA analyses (black), and their fits using model structures containing multiple Au–Au pairs (red). As fitting parameters, we considered three Au–Au pairs for the S_0, S_1 and T_1 state, and six Au–Au pairs for the tetramer. Reprinted by permission from Macmillan Publishers Ltd: *Nature* (ref. 15), copyright (2015).

Table 13.1 Kinetic parameters determined from the data analysis.

	S_1 to T_1	T_1 to tetramer	Tetramer to S_0
Time constant	1.6 ± 0.1 ps	3 ± 0.5 ns	100 ± 20 ns

Table 13.2 Structural parameters of the reaction intermediates determined from the data analysis.

Species	R_{12} (Å)	R_{23} (Å)	R_{13} (Å)	R_{34} (Å)
S_0	3.87 ± 0.04	3.30 ± 0.06	5.56 ± 0.11	-
S_1 (T_1')	2.82 ± 0.04	2.81 ± 0.03	5.63 ± 0.09	-
T_1	2.71 ± 0.03	2.70 ± 0.05	5.41 ± 0.11	-
Tetramer	2.89 ± 0.06	2.62 ± 0.06	-	2.88 ± 0.04

S_0, S_1, T_1 and tetramer states in Figure 13.4B are in good agreement with the results of the previous theoretical calculation.[14]

The previous TA study identified the changes of transient absorption on 500 fs, 2 ps and 2 ns time scales.[12] Based on the measured time constants and the theoretical electronic absorption spectra, the following mechanism was suggested for the Au–Au bond formation in $[Au(CN)_2^-]_3$. The S_1 state is rapidly populated within a few hundred femtoseconds accompanying contraction of the Au–Au bonds, but without any bent-to-linear transition. Subsequently, the T_1 state of a linear staggered structure is formed in 2 ps *via* the bent-to-linear transition, and then the trimer associates with a free monomer to form a tetramer in 2 ns. The time scales of the transitions found in the TA study match well with the results of this work, but the detailed structural changes were assigned differently. In particular, from our TRXL measurement and analysis, the bent-to-linear transition was found to occur within a few hundred femtoseconds rather than on the time scale of 2 ps.

To account for this discrepancy, we determined the structure of the S_1 state more carefully by fitting the experimental difference scattering curve at 200 fs time delay using two different model structures as shown in Figure 13.5. One is a linear structure where R_{13} is equal to the sum of R_{12} and R_{23}, and the other is a bent structure where the Au–Au–Au bond angle of the S_0 state is preserved for the S_1 state. In Figure 13.5A, it is clearly seen that the theoretical scattering curve calculated from the linear structure (χ^2 = 1.70) fits the experimental scattering curve at the 200 fs time delay much better than the one calculated from the bent structure (χ^2 = 4.81). The difference between the linear and bent structures can be seen more distinctly in the RDFs in *r*-space shown in Figure 13.5B. In the bent structure, R_{13} is too small to fit the experimental RDF at 200 fs. Therefore, the bent-to-linear transition must be completed at 200 fs time delay.

Based on the reconstructed structures of the four different states and the transition dynamics among them, we summarized the mechanism for photoinduced formation of Au–Au covalent bonds in $[Au(CN)_2^-]_3$ in Figure 13.6 with the assignments of kinetics from the TA and TRXSS studies. The S_0 state with weakly bound Au atoms in a bent geometry transforms within a few hundred femtoseconds to the S_1 state with tightly bound Au atoms (2.8 Å Au–Au distances) in a linear and symmetric geometry. The S_1 state transforms to the T_1 state with 1.6 ps time constant accompanying further contraction of Au–Au bonds by 0.1 Å. Then, the T_1 state converts to a tetramer in 3 ns *via*

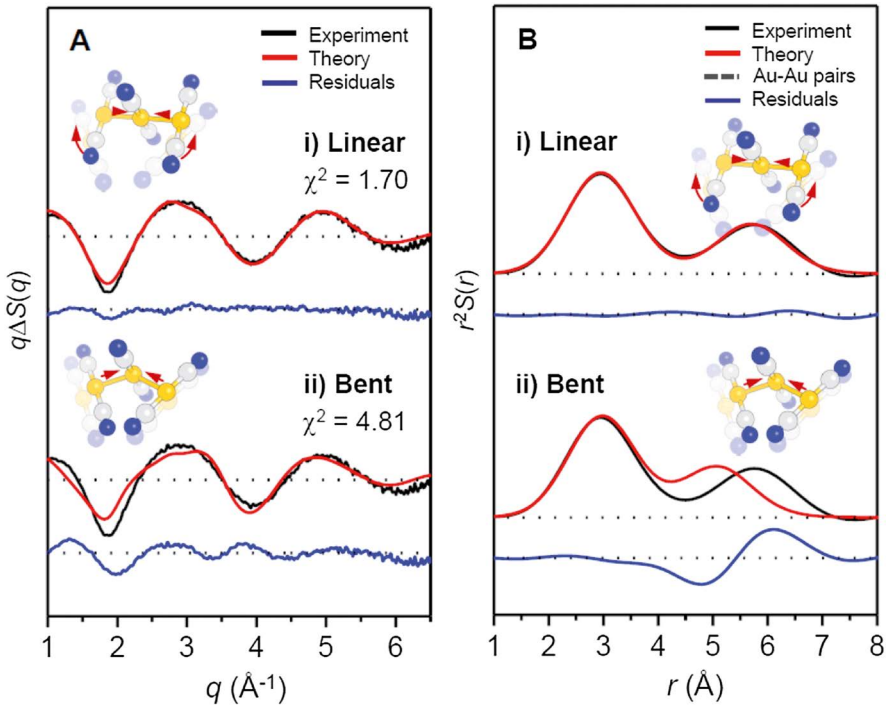

Figure 13.5 Structure determination of the S_1 state using the experimental scattering curve at 200 fs time delay in *q*-space and *r*-space. (A) Theoretical difference scattering curves (red) for linear (upper) and bent (lower) structures shown together with the experimental difference scattering curve at 200 fs (black). The residuals (blue) between the theoretical and the experimental curves are shown together. The linear structure gives a much better fit than the bent structure, which has the same Au–Au–Au bond angle as the S_0 state, thereby indicating that the bent-to-linear transition is completed at the 200 fs time delay. (B) Corresponding experimental (black) and theoretical (red) radial distribution functions, $rS(r)$. It can be seen that, in the bent structure, R_{13} is too small to fit the experimental RDF at 200 fs. Reprinted by permission from Macmillan Publishers Ltd: *Nature* (ref. 15), copyright (2015).

formation of another Au–Au bond and, ultimately, the S_0 state is recovered in ~100 ns. Considering that TRXL is only sensitive to the processes accompanying structural change, the intersystem crossing processes on ~500 fs and 13 ns time scales, which were not observed in the TRXL measurement, are likely to involve no structural change.

13.4 Conclusion

Here, we demonstrated the capability of femtosecond TRXL provided by an XFEL facility by elucidating the overall mechanism for the formation of Au–Au covalent bonds in the $[Au(CN)_2^-]_3$ complex with rich structural information.

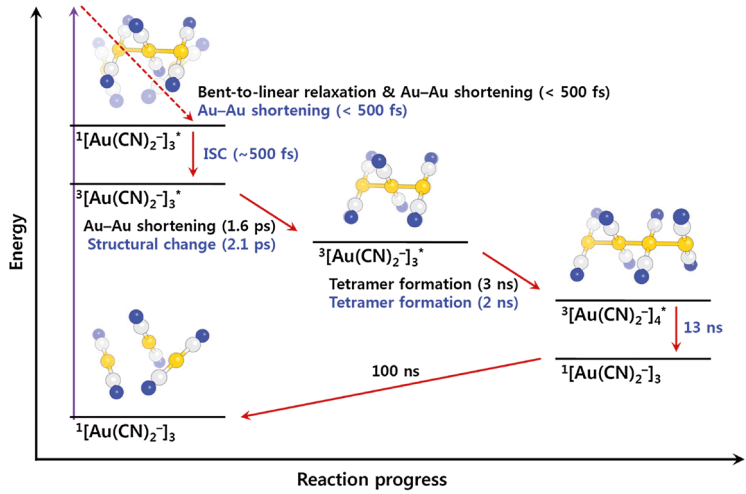

Figure 13.6 Mechanism of photoinduced bond formation in $[Au(CN)_2^-]_3$. Femtosecond TRXL reveals the dynamics and the atomic movements associated with the Au–Au bond formation in real time with sub-angstrom spatial resolution. Mechanism of photoinduced bond formation in $[Au(CN)_2^-]_3$. Results from our TRXL data (red) and previous TA experiment (blue) are shown together. The S_0 state with weakly bound Au atoms in a bent geometry transforms to the S_1 state with tightly bound Au atoms in a linear geometry. Subsequently, the S_1 state transforms to the T_1 state accompanying further contraction of Au–Au bonds and then to a tetramer *via* formation of another Au–Au bond. Our findings are in good agreement with the reaction mechanism proposed in the TA study, except for the structural assignments of the early kinetics. Reprinted by permission from Macmillan Publishers Ltd: *Nature* (ref. 15), copyright (2015).

AQ1

AQ1: Yes. It should read "Results from our TRXL data (black) and previous TA experiment (blue) are shown together".

Femtosecond TRXL offers the opportunity to visualize the entire process of photoinduced reactions in real time and real space, and can be used as a fundamental tool for studying the reaction dynamics of chemical and biological systems.

Acknowledgements

We thank Prof. Munetaka Iwamura, Prof. Koichi Nozaki, Dr Satoshi Takeuchi and Dr Tahei Tahara for helpful discussions. This work was supported by IBS-R004-G2, the X-ray Free Electron Laser Priority Strategic Program of MEXT, the Innovative Areas "Artificial Photosynthesis (AnApple)" (no. 25107527) grant from the Japan Society for the Promotion of Science (JSPS), and Basic Science Research Program through the National Research Foundation of Korea (NRF) funded by the Ministry of Science, ICT & Future Planning (NRF-2014R1A1A1002511). The experiments were performed at the BL3 of SACLA with the approval of the Japan Synchrotron Radiation

Research Institute (JASRI) (Proposal No. 2012A8030, 2012A8038, 2012B8029, 2012B8043, 2013A8053, 2013B8036, 2013B8059, 2014A8042, 2014A8022 and 2015B8055) and at the NW14A of KEK with the approval of the Photon Factory Program Advisory Committee (Proposal No. 2011G655, 2012G778 and 2012G779).

References

1. A. H. Zewail, *Science*, 1988, **242**, 1645.
2. A. L. Harris, J. K. Brown and C. B. Harris, *Annu. Rev. Phys. Chem.*, 1988, **39**, 341.
3. D. M. Jonas, S. E. Bradforth, S. A. Passino and G. R. Fleming, *J. Phys. Chem.*, 1995, **99**, 2594.
4. A. H. Zewail, *Angew. Chem., Int. Ed.*, 2001, **40**, 4371.
5. M. Wall, A. N. Tarnovsky, T. Pascher, V. Sundstrom and E. Akesson, *J. Phys. Chem. A*, 2003, **107**, 211.
6. M. A. Rawashdeh-Omary, C. L. Larochelle and H. H. Patterson, *Inorg. Chem.*, 2000, **39**, 4527.
7. M. A. Rawashdeh-Omary, M. A. Omary, H. H. Patterson and J. P. Fackler, *J. Am. Chem. Soc.*, 2001, **123**, 11237.
8. P. Pyykko, *Angew. Chem., Int. Ed.*, 2004, **43**, 4412.
9. M. A. Rawashdeh-Omary, M. A. Omary and H. H. Patterson, *J. Am. Chem. Soc.*, 2000, **122**, 10371.
10. S. G. Wang and W. H. E. Schwarz, *J. Am. Chem. Soc.*, 2004, **126**, 1266.
11. H. Schmidbaur and A. Schier, *Chem. Soc. Rev.*, 2008, **37**, 1931.
12. M. Iwamura, K. Nozaki, S. Takeuchi and T. Tahara, *J. Am. Chem. Soc.*, 2013, **135**, 538.
13. M. Iwamura, R. Wakabayashi, J. Maeba, K. Nozaki, S. Takeuchi and T. Tahara, *Phys. Chem. Chem. Phys.*, 2016, **18**, 5103.
14. G. L. Cui, X. Y. Cao, W. H. Fang, M. Dolg and W. Thiel, *Angew. Chem., Int. Ed.*, 2013, **52**, 10281.
15. K. H. Kim, J. G. Kim and S. Nozawa, *et al.*, *Nature*, 2015, **518**, 385.
16. K. H. Kim, J. G. Kim and K. Y. Oang, *et al.*, *Struct. Dyn.*, 2016, **3**, 043209.
17. E. Collet, M. H. Lemee-Cailleau and M. Buron-Le Cointe, *et al.*, *Science*, 2013, **300**, 612.
18. K. Sokolowski-Tinten, C. Blome and J. Blums, *et al.*, *Nature*, 2003, **422**, 287.
19. F. Schotte, M. Lim and T. A. Jackson, *et al.*, *Science*, 2003, **300**, 1944.
20. H. Ihee, S. Rajagopal and V. Srajer, *et al.*, *Proc. Natl. Acad. Sci.*, 2005, **102**, 7145.
21. D. M. Fritz, D. A. Reis and B. Adams, *et al.*, *Science*, 2007, **315**, 633.
22. P. Coppens, *J. Phys. Chem. Lett.*, 2011, **2**, 616.
23. T. A. Miller, J. S. Wittenberg, H. Wen, S. Connor, Y. Cui and A. M. Lindenberg, *Nat. Commun.*, 2013, **4**, 1369.
24. Y. O. Jung, J. H. Lee, J. Kim, M. Schmidt, K. Moffat, V. Srajer and H. Ihee, *Nat. Chem.*, 2013, **5**, 212.

AQ2: A. Plech, V. Kotaidis, M. Lorenc and J. Boneberg, Nat. Phys., 2006, 2, 44.

25. H. Ihee, M. Lorenc and T. K. Kim, *et al.*, *Science*, 2005, **309**, 1223.
26. J. Davidsson, J. Poulsen and M. Cammarata, *et al.*, *Phys. Rev. Lett.*, 2005, **94**, 245503.
27. A. Plech, K. V. , M. Lorenc and J. Boneberg, *Nat. Phys.*, 2006, **2**, 44.
28. J. Vincent, M. Andersson and M. Eklund, *et al.*, *J. Chem. Phys.*, 2009, **130**, 154502.
29. M. Christensen, K. Haldrup and K. Bechgaard, *et al.*, *J. Am. Chem. Soc.*, 2009, **131**, 502.
30. H. Ihee, *Acc. Chem. Res.*, 2009, **42**, 356.
31. K. Haldrup, M. Christensen and M. Cammarata, *et al.*, *Angew. Chem., Int. Ed.*, 2009, **48**, 4180.
32. T. K. Kim, J. H. Lee, M. Wulff, Q. Kong and H. Ihee, *ChemPhysChem*, 2009, **10**, 1958.
33. M. Christensen, K. Haldrup and K. S. Kjaer, *et al.*, *Phys. Chem. Chem. Phys.*, 2010, **12**, 6921.
34. H. Ihee, M. Wulff, J. Kim and S. Adachi, *Int. Rev. Phys. Chem.*, 2010, **29**, 453.
35. K. Haldrup, T. Harlang and M. Christensen, *et al.*, *Inorg. Chem.*, 2011, **50**, 9329.
36. K. Haldrup, G. Vanko and W. Gawelda, *et al.*, *J. Phys. Chem. A*, 2012, **116**, 9878.
37. K. H. Kim, J. H. Lee and J. Kim, *et al.*, *Phys. Rev. Lett.*, 2013, **110**, 165505.
38. K. H. Kim, J. Kim, J. H. Lee and H. Ihee, *Struct. Dyn.*, 2014, **1**, 011301.
39. S. E. Canton, K. S. Kjær and G. Vankó, *et al.*, *Nat. Commun.*, 2015, **6**, 6359.
40. M. Cammarata, M. Levantino and F. Schotte, *et al.*, *Nat. Methods*, 2008, **5**, 988.
41. M. Andersson, E. Malmerberg and S. Westenhoff, *et al.*, *Structure*, 2009, **17**, 1265.
42. H. S. Cho, N. Dashdorj, F. Schotte, T. Graber, R. Henning and P. Anfinrud, *Proc. Natl. Acad. Sci. U. S. A.*, 2010, **107**, 7281.
43. K. H. Kim, S. Muniyappan and K. Y. Oang, *et al.*, *J. Am. Chem. Soc.*, 2012, **134**, 7001.
44. K. Y. Oang, J. G. Kim and C. Yang, *et al.*, *J. Phys. Chem. Lett.*, 2014, **5**, 804.
45. J. G. Kim, T. W. Kim, J. Kim and H. Ihee, *Acc. Chem. Res.*, 2015, **48**, 2200.
46. D. Arnlund, L. C. Johansson and C. Wickstrand, *et al.*, *Nat. Methods*, 2014, **11**, 923.
47. E. Malmerberg, P. H. M. Bovee-Geurts and G. Katona, *et al.*, *Sci. Signaling*, 2015, **8**, ra26.
48. M. Levantino, G. Schiro and H. T. Lemke, *et al.*, *Nat. Commun.*, 2015, **6**, 6772.
49. T. W. Kim, C. Yang and Y. Kim, *et al.*, *Phys. Chem. Chem. Phys.*, 2016, **18**, 8911.
50. Y. Inubushi, K. Tono and T. Togashi, *et al.*, *Phys. Rev. Lett.*, 2012, **109**, 144801.
51. T. Ishikawa, H. Aoyagi and T. Asaka, *et al.*, *Nat. Photonics*, 2012, **6**, 540.
52. M. Harmand, R. Coffee and M. R. Bionta, *et al.*, *Nat. Photonics*, 2013, **7**, 215.

53. T. Katayama, Y. Inubushi and Y. Obara, *et al.*, *Appl. Phys. Lett.*, 2013, **103**, 131105.
54. H. T. Lemke, C. Bressler and L. X. Chen, *et al.*, *J. Phys. Chem. A*, 2013, **117**, 735.
55. M. G. Jones, Y. Bessho and S. Kim, *et al.*, *Nat. Commun.*, 2014, **5**, 3798.
56. K. Tamasaku, E. Shigemasa and Y. Inubushi, *et al.*, *Nat. Photonics*, 2014, **8**, 313.
57. W. Zhang, R. Alonso-Mori and U. Bergmann, *et al.*, *Nature*, 2014, **509**, 345.
58. Y. D. Chuang, W. S. Lee and Y. F. Kung, *et al.*, *Phys. Rev. Lett.*, 2013, **110**, 127404.